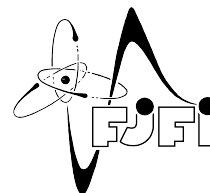




ČESKÉ VYSOKÉ UČENÍ TECHNICKÉ V PRAZE  
Fakulta jaderná a fyzikálně inženýrská



# Experiment s tekutým lithiem a cínom na divertoru tokamaku COMPASS

## Experiment with liquid lithium and tin on tokamak COMPASS divertor

Výzkumný úkol  
Research Assignment

Autor: **Jan Čečrdle**  
Vedoucí práce: **Mgr. Jan Horáček, Dr. és sc.**  
Akademický rok: 2019/2020

*Název práce:*

## **Experiment s tekutým lithiem a cínem na divertoru tokamaku COMPASS**

*Autor:* Jan Čečrdle

*Obor:* Fyzika a technika termojaderné fúze

*Druh práce:* Výzkumný úkol

*Vedoucí práce:* Mgr. Jan Horáček, Dr. és sc., Ústav fyziky plazmatu AV ČR, v.v.i.

*Abstrakt:*

Tekuté kovy představují potenciální řešení problému přehřívání divertoru tokamaků. Tento problém bude obzvláště u velkých zařízení s fúzním výkonem v řádech stovek MW, jako například ITER nebo DEMO, klíčový. Nutnost využití kovových materiálů, wolframu a berylia, stanovuje limit na maximální tepelné toky a tepelné šoky, které jsou z inženýrského hlediska přijatelné. Tekuté kovy jsou schopné tyto limity posunout na dostatečnou úroveň, nutnou pro bezpečný provoz reaktoru. Překážkou v použití tekutých kovů je ovšem problém konstrukce stěn z těchto materiálů, zachytávání paliva (tritia) a také možné výrazné unikání materiálu do plazmatu. Jedním z možných způsobů konstrukce stěny s tekutým kovem je technologie CPS (kapilární porézní struktura). Tato práce se zabývá experimentem s tekutými kovy (lithiem a cín-lithiovou slitinou) na tokamaku COMPASS a jeho simulováním. Cílem experimentu bylo stanovení možnosti použití technologie CPS v plazmatu s divertorovou konfigurací typu ITER.

*Klíčová slova:* tokamak, COMPASS, divertor, tekuté kovy, kapilární porézní systém, litium, cín

*Title:*

## **Experiment with liquid lithium and tin on tokamak COMPASS divertor**

*Author:* Jan Čečrdle

*Abstract:*

Liquid metals provide potential solution of the problem of tokamak divertors overheating. This problem will be apparent in large tokamaks with high fusion power output (in orders of hundreds of MW), such as ITER or DEMO. The necessity of usage of metallic materials (tungsten and beryllium), provides maximal heat fluxes and heat shocks, acceptable in engineering perspective of tokamak vessel construction. Liquid metals could shift these limits into acceptable ranges for safe operation of said reactors. An obstacle in usage of liquid metals is the construction of walls with these materials, fuel (tritium) retention and potential release into plasma. One option of liquid wall construction is the CPS (Capillary porous structure) technology. This assignment deals with liquid metals experiment at the COMPASS tokamak and its simulations. The task of this experiment was the evaluation of possible implementation of CPS into divertors in ITER like tokamaks.

*Key words:* tokamak, COMPASS, divertor, liquid metals, capillary porous system, lithium, tin



# Contents

<b>1</b>	<b>Plasma Physics</b>	<b>5</b>
1.1	Plasma facing components . . . . .	5
1.1.1	ITER First Wall . . . . .	5
1.1.2	ITER Divertor . . . . .	6
1.2	Transient heat events . . . . .	6
1.2.1	Edge Localised Modes . . . . .	6
1.3	Liquid metals . . . . .	8
1.3.1	Capillary Porous Structure . . . . .	8
1.4	Magneto-hydrodynamics . . . . .	8
1.4.1	Rayleigh-Taylor Instability . . . . .	9
1.4.2	Kelvin-Helmholtz Instability . . . . .	9
<b>2</b>	<b>CPS experiments on COMPASS tokamak</b>	<b>10</b>
2.1	Overview of the experiments . . . . .	10
2.2	Experimental results . . . . .	12
2.2.1	Lithium target . . . . .	12
2.2.2	Tin-lithium target . . . . .	14
<b>3</b>	<b>Vapor shielding model</b>	<b>16</b>
3.1	3D Heat Transport model . . . . .	16
3.1.1	Thermal diffusion . . . . .	16
3.1.2	Vapor cooling effects . . . . .	16
3.2	Corrections in the model . . . . .	17
3.2.1	Vapor Cooling . . . . .	17
3.2.2	Lithium prompt Redeposition . . . . .	18
3.3	Tin-lithium experiment simulations . . . . .	18
3.4	Simulation of discharge #19925 and comparison with experimental results . . . . .	20
<b>4</b>	<b>Conclusion</b>	<b>23</b>
<b>5</b>	<b>Attachment</b>	<b>24</b>
	<b>Literature</b>	<b>27</b>

# Introduction

Recent study of plasma induced heat fluxes on plasma facing components in large tokamaks with divertor configuration such as ITER or DEMO show, that current technological solutions might not be sufficient for safe operations. For steady state heat flux to be in acceptable range, detachment operation mode is assumed for ITER. This poses high importance on precise feedback control. If the currently uncertain conditions influencing heat flux, such as flux expansion, are taken into consideration, a considerable risk for PFC lifespan arises. The problem of PFC damaging due to high heat fluxes and heat shocks (cracking, melting, quenching etc.) is even more imminent when transient heat events are taken into account. In divertor tokamaks such as ITER or DEMO these include edge localized modes, vertical displacement events and disruptions. However because disruptions are accompanied by strong forces capable of severely damaging the reactor vessel itself, the threat inflicted on PFC is minuscule in comparison.

With the aim to solve the overheating problem, the idea of a liquid plasma facing component has been proposed as early as 1994. [8]. The research of LMD technologies has been accelerated in recent years as a result of the problem of wolfram made divertor operation under heavy heat load [23, 41, 24]. Several solutions how to incorporate liquefied metals into PFCs have been tested. One of the most promising ones is so called capillary porous structure. In this technology the liquid metal is held in place and refilled if drained by capillary forces in a porous material (mesh, felt etc.) with high thermal resistance. If the temperature of the surface exceeds the boiling point of the liquid component, firstly all of the liquid is boiled away and only after that the temperature continues to rise. This phenomenon makes a robust fail-safe mechanism, especially for sudden heat flux spikes and large heat shocks. This assignment deals with the first experiment with liquid metals (Li and SnLi alloy) at the COMPASS tokamak. In the first chapter, theoretical background on PFC physics, transient heat events, liquid metals and MHD instabilities is presented. The liquid metal divertor (LMD) experiments conducted in COMPASS tokamak are discussed in the second chapter. In the third chapter, the 3D heat conduction and vapor cooling model presented in [1] is briefly summarized and corrections done with new results and knowledge are presented. In the last chapter the work done is summarized and conclusions are made.

# 1. Plasma Physics

## 1.1 Plasma facing components

Plasma facing components are those components of a plasma device, that are in direct contact with the plasma. As such they are subjects to high energy particle fluxes, high heat fluxes, high electrical currents and other phenomena that can be potentially dangerous and destructive to the PFCs. For this reason there is an extensive endeavor to develop advanced materials capable of withstanding these extreme conditions. In case of a tokamak PFCs contain the first wall, limiters and/or the divertor.

### 1.1.1 ITER First Wall

The ITER first wall will be constructed from beryllium covered panels (Fig. 1.1). The usage of beryllium for the first wall is the low  $Z$  requirement, due to the proximity of separatrix and potential release of the material into the core plasma. The "Enhanced heat flux" FW design utilizing CuCrZr made heat sink with a hyper-vapotron based active cooling is capable of handling heat fluxes up to  $4.7 \text{ MW/m}^2$ . This is sufficient for ITER operation as the bulk of the total incoming heat flux from the plasma will be deposited on the divertor. The only situations when considerable heat load is deposited on the first wall is in the ramp up phase, before X-point formation (and ramp down phase), or transient events such as vertical displacement events (VDE) and disruptions [12].

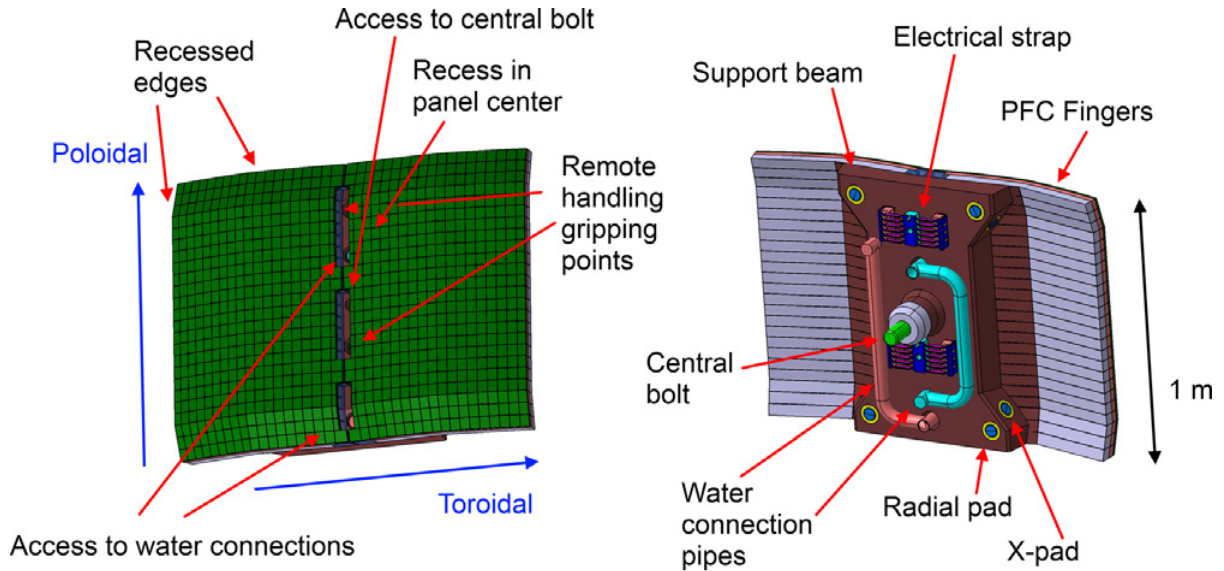


**Fig. 1.1:** Design of a ITER first wall panel (Blanket Module 1). Taken from [12].

### 1.1.2 ITER Divertor

As the power deposited on the divertor is expected to be up to  $20 \text{ MW/m}^2$  [23] in steady state attached plasma, the possible materials for ITER divertor must have high heat load resistance. Because of high fuel retention and high sputtering, graphite, which could withstand these heat loads, is not a viable option. For these reasons tungsten was chosen as the divertor plasma facing material. The resulting design is shown in Fig. 1.2. The concerning issue of this design is the possible cracking (at  $20 \text{ MW/m}^2$ ), local melting and overall degradation of the tungsten plasma facing units. ITER operation especially in the fusion regime, with additional 500 MW of fusion power, could result in frequent impairment of the tiles resulting in more difficult operation caused by necessary repairs. This problem would be even more apparent in DEMO reactor, as heat loads would be considerably higher and frequent repairs of the divertor would decrease the economical viability of the plant [23, 11, 19, 20].

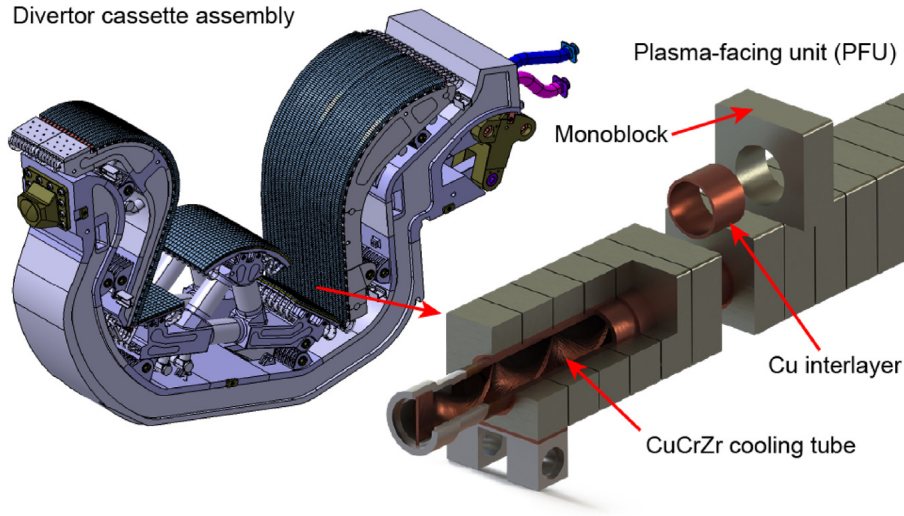


**Fig. 1.2:** ITER divertor cassette CAD model with the tungsten monoblock and CuCrZr cooling pipes close up. Taken from [11]

## 1.2 Transient heat events

Apart from steady state heat flux, so called transient heat events must be taken into account, when designing plasma facing components and their cooling. Even though they are short in duration, these events can create high enough heat loads and thermal shocks, to irreversibly damage PFCs. In tokamaks with divertor configuration these include ELMs, VDE and disruptions, each with specific duration and heat load. This problem is more apparent in larger devices especially with generation of fusion power, such as ITER, DEMO or future power plants based on the same design.

### 1.2.1 Edge Localised Modes

Edge localized modes are periodical magneto-hydrodynamical instabilities occurring in tokamak plasmas in H-mode operation regime. This regime occurs when total heating power exceeds a threshold value. Edge transport barrier, which is present in H-modes, results in accumulation of

energy in confined plasma, which is then periodically released into SOL resulting in characteristic spiking in measured quantities ( $H_\alpha$  radiation, heat flux, density and others).

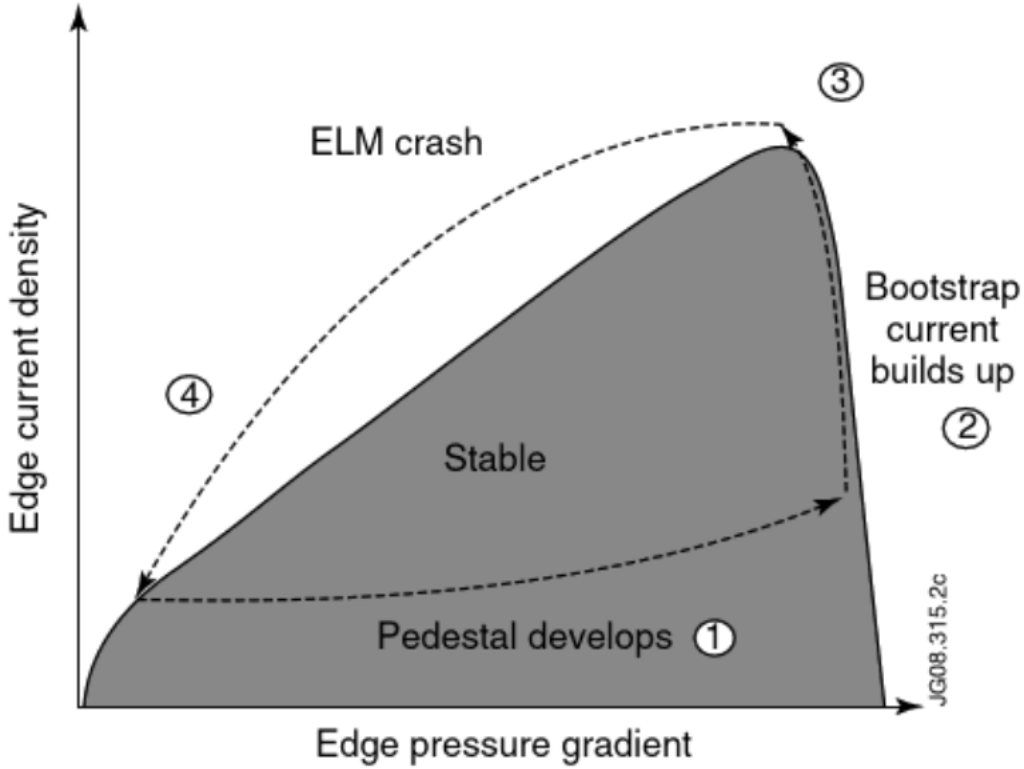


**Fig. 1.3:** Diagram of the ELM cycle in the peeling ballooning graph of tokamak edge stability. Taken from [9].

When the edge transport barrier is created due to L-H transition, a steep pressure gradient (pedestal) forms. With further heating the pressure gradient increases to the ballooning limit (Section 1 in Fig. 1.3). Following build up of edge current density (Sec. 2 in Fig. 1.3), due to Ohmic and bootstrap currents shifts the edge plasma parameters to the upper right corner of the stability boundary (Sec. 3 in Fig. 1.3), resulting in ELM crash (Sec. 4 in Fig. 1.3). The cycle is then repeated [9].

There are three types of ELMs distinguished by dependence of repetition frequency  $\nu_{\text{elm}}$  and power crossing the separatrix  $P_{\text{sep}}$ . This dependence is used to for identification of Type I and Type III ELMs for  $\frac{d\nu_{\text{elm}}}{dP_{\text{sep}}} > 0$  and  $\frac{d\nu_{\text{elm}}}{dP_{\text{sep}}} < 0$  respectively. In case of Type II ELMs no apparent dependence of  $\nu_{\text{elm}}$  and  $P_{\text{sep}}$  is observed. Type II ELMs are usually present in strongly shaped plasmas. Type III ELMs typically occur close to L-H transition threshold. In current devices ELM crash time is in range of hundreds of microseconds to few milliseconds [9].

The predicted heat shocks of ITER ELMs is  $66 \text{ MJm}^{-2}\text{s}^{-1/2}$  [23]. This is enough to locally melt the wolfram monoblock plasma facing units. Mitigation, suppression or other form of lowering the heat shock of the ELMs or new divertor design is therefore required [23, 20].

## 1.3 Liquid metals

The term "liquid metal" can be broadly applied to any metallic compound in a liquid state of matter. However in tokamak physics, this term is used for materials, that are in liquid state in the range of operational conditions of the device (i.e. high vacuum and temperatures in lower hundreds of degrees Celsius). Liquid metals, or alloys, can be used in tokamaks and tokamak based power plants in variety of applications. For example as coolants or fuel breeding media. Liquid metals can be also used as plasma facing components, which is the topic of this assignment. The advantage of a liquid plasma facing surface is the absence of a crystalline lattice. However each of the potential materials usable as a plasma facing material has its disadvantages, such as fuel retention in case of lithium or high Z in case of tin. An obstacle all liquid metals share is fluidity. This property makes all efforts of designing PFCs based on liquid metals challenging.

### 1.3.1 Capillary Porous Structure

Capillary porous structure (CPS) is a technology utilizing capillary forces to hold a wetting liquid in a solid mesh. In tokamaks this can be used as a support structure in the construction of a liquid plasma facing component (mainly the divertor). If subjected to a high heat flux, the temperature of the CPS component rises up to the boiling point of the liquid and rises further only after the liquid is boiled away, as demonstrated by several experiments in linear devices and tokamaks (Fig. 1.4). This effect could protect the currently used tungsten based divertors from high temperature rises resulting in the damage of the PFCs. The present liquid in the vacuum vessel in a plasma device also has several disadvantages, such as high particle release, due to sputtering and evaporation. In case of lithium, a potential liquid metal usable in tokamak PFC design another obstacle is potential fuel retention [30, 36, 49].

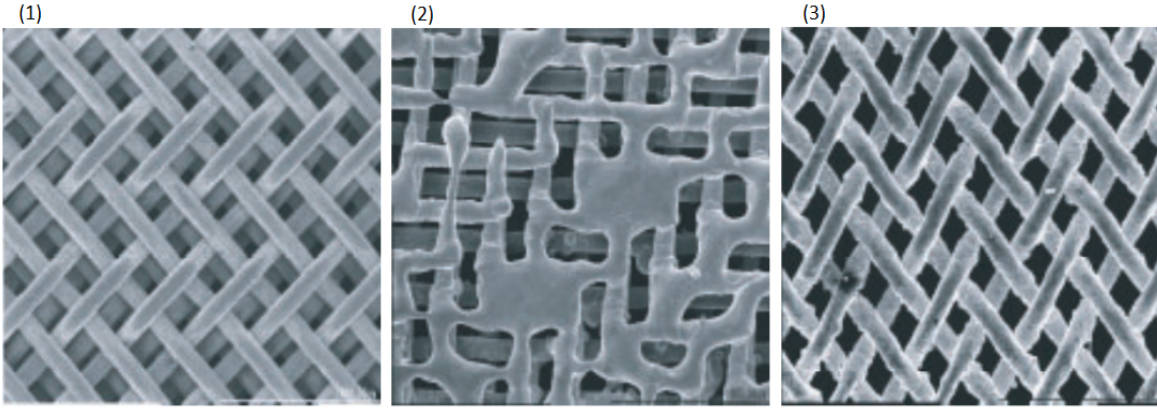


**Fig. 1.4:** Photographs of the CPS mesh (1) CPS wetted with Li, (2) CPS without Li after one discharge of energy  $Q = 4\text{MJ/m}^2$ , and duration  $t = 250\text{ }\mu\text{s}$ , (3) CPS with lithium after 22 discharges. Taken from [29].

## 1.4 Magneto-hydrodynamics

Description of plasma as a single fluid model is done via magneto-hydrodynamics. Plasma is there for simplicity taken as one fluid and its behavior is calculated through the Maxwell's equations and the Navier-Stokes equation. This approximation is accurate in plasmas with high collisionality

and with Maxwell-Boltzmann velocity distribution or a distribution close to it. Maxwell's equations are

$$\nabla \cdot \mathbf{D} = \rho_q, \quad (1.1a)$$

$$\nabla \cdot \mathbf{B} = 0, \quad (1.1b)$$

$$\nabla \times \mathbf{E} = -\frac{\partial \mathbf{B}}{\partial t}, \quad (1.1c)$$

$$\nabla \times \mathbf{H} = \mathbf{j} + \frac{\partial \mathbf{D}}{\partial t}, \quad (1.1d)$$

where  $\mathbf{D}$  is electric induction,  $\mathbf{B}$  is magnetic flux density,  $\mathbf{E}$  is electric field intensity,  $\mathbf{H}$  is magnetic field intensity,  $\rho_q$  is charge density and  $\mathbf{j}$  is electric current density. And the Navier-Stokes equation in conservation form is

$$\rho \frac{\partial \mathbf{u}}{\partial t} + \rho(\mathbf{u} \cdot \nabla) \mathbf{u} = -\nabla p + \eta \nabla^2 \mathbf{u} + \left(\zeta + \frac{\eta}{3}\right) \nabla(\text{div} \mathbf{u}) + \mathbf{j} \times \mathbf{B}, \quad (1.2)$$

where  $\mathbf{u}$  is flow velocity,  $\rho$  is density,  $p$  is pressure,  $\eta$  and  $\zeta$  are first and second viscosities [13].

#### 1.4.1 Rayleigh-Taylor Instability

Rayleigh-Taylor instability [13, 5] develops at an interface of two fluids, where the density gradient has an opposite direction to an acting force (for example a denser fluid above a thinner fluid in gravity field). For a plane interface the dispersion relation is

$$\omega^2(\rho_a + \rho_b) - \frac{1}{\mu_0} [(\mathbf{k} \cdot \mathbf{B}_a)^2 + (\mathbf{k} \cdot \mathbf{B}_b)^2] + gk(\rho_a - \rho_b) = 0, \quad (1.3)$$

where  $\mu_0$  is vacuum permeability,  $g$  is gravitational acceleration,  $\rho_{a,b}$  are densities,  $\mathbf{B}_{a,b}$  are magnetic fields and  $\mathbf{u}_{a,b}$  are the speeds of the respective fluids.  $\mathbf{k}$  is the wave number and  $\omega$  is the frequency of the instability.

#### 1.4.2 Kelvin-Helmholtz Instability

Kelvin-Helmholtz instability [13, 5] generally occurs at an interface of two fluids with a speed difference or in a continuous fluid with a sheer velocity gradient. The general dispersion relation for a plane interface is

$$(\omega - \mathbf{k} \cdot \mathbf{u}_a)^2 \rho_a + (\omega - \mathbf{k} \cdot \mathbf{u}_b)^2 \rho_b - \frac{1}{\mu_0} [(\mathbf{k} \cdot \mathbf{B}_a)^2 + (\mathbf{k} \cdot \mathbf{B}_b)^2] + gk(\rho_b - \rho_a) = 0. \quad (1.4)$$

## 2. CPS experiments on COMPASS tokamak

### 2.1 Overview of the experiments

With the goal of testing viability of CPS technology in diverted plasmas, especially in ELMy H-mode, experimental campaigns with pure lithium and tin-lithium alloy (27% Li and 73% Sn) filled CPS targets were conducted in COMPASS tokamak. The first module was a  $45 \times 20 \times 24$  mm molybdenum block covered with molybdenum mesh. The wire width of the mesh is  $100 \mu\text{m}$  and pore size is  $75 \mu\text{m}$ . Several layers of the mesh were wound on the block with the total width of the porous segment of 1 mm (ref fig). The interior of the the block contained a reservoir for additional liquid metal. The second module, wetted with SnLi alloy was identical to the first one in dimensions and used mesh, however the bulk was constructed from boron-nitride-carbide providing lower heat conduction from the surface and the porous mat to ensure higher surface temperatures (Molybdenum heat conductivity is  $\kappa_{\text{Mo}} = 145 - T[^\circ\text{C}]/33$  W/m/K [2] and BNC conductivity is  $\kappa_{\text{BNC}} \approx 17$  W/m/K). Both targets were equipped with a 50W heater used for preheating to sufficient temperatures for melting the wetting metals,  $180^\circ\text{C}$  for pure Li and  $330^\circ\text{C}$  for SnLi alloy, and two thermal resistors for temperature measurements inside the targets [1, 2, 3].

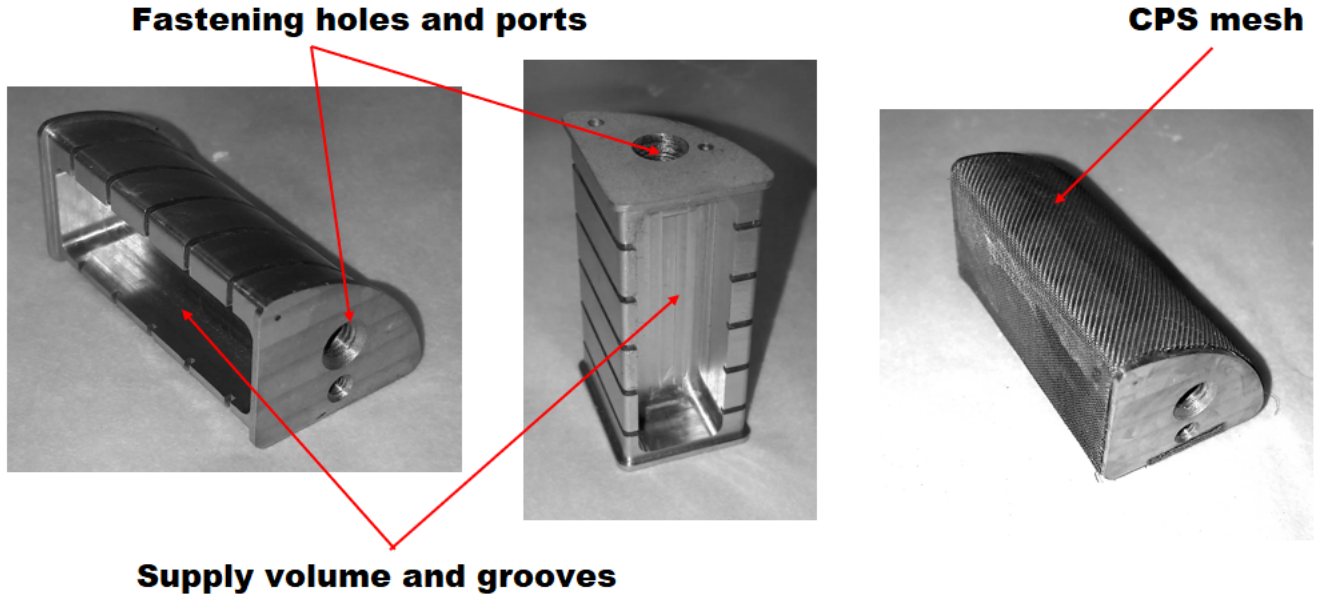


**Fig. 2.1:** Photographs of the molybdenum block, showing the reservoir, supply grooves and ports and the 1 mm Mo mesh covering the block.



The targets were placed in a vertical port at the high field side of the COMPASS divertor (Fig. 2.2). The manipulator the targets were installed at provided a  $z = 0-7.5$  mm insertion above the divertor tiles. Combined with the cylindrical shape of the plasma facing surface of the target with radius  $r = 22$  mm, it creates a possibility of a variable heat load on the target raising with the insertion height as

$$q = q_{\parallel} \sin(\alpha), \quad (2.1a)$$

$$\sin(\alpha) = \frac{\sqrt{(r^2 - (r - z)^2)}}{r}. \quad (2.1b)$$

Due to the geometry of the plasma facing surface of the target and incoming flux lines, the largest heat flux achieved is at the bottom of the inserted part (Fig. 2.2c). The surrounding divertor tiles create a magnetic shade on the target. The shape of the shade is approximately parabolic, due to the shape of the divertor tiles. This is very important for discharges with small insertion, as the shape of the shadow can effect the heat flux drastically. Another problem for discharges with small insertion is the uncertainty of the target inclination caused by imprecise installation. The inclination would also effect resulting heat flux.

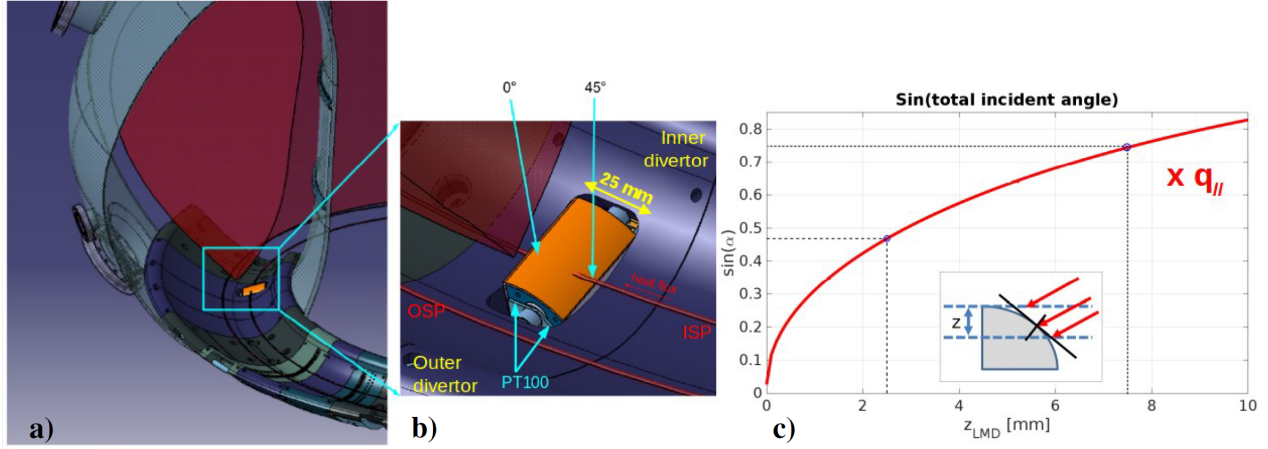


**Fig. 2.2:** a) CAD model of the COMPASS chamber with the position of the LMD target. b) Zoomed view of the target c) Graph and diagram of the variation of incident angle of field lines as a function of insertion height  $z$ . Taken from [3].

The parameters of the discharges the targets were exposed are: toroidal magnetic field  $B_t = 1.4$  T, plasma current  $I_p = 230$  kA, line averaged density  $n_L = 2-3 \cdot 10^{19} \text{ m}^{-3}$  in L-mode,  $n_H = 4.5 \cdot 10^{19} \text{ m}^{-3}$  in H-mode with flattop duration of  $t^{ft} = 150-250$  ms. The resulting parallel heat flux at the inner strike point is  $q_{\parallel} = 20-30 \text{ MW/m}^2$ , measured by divertor probes and infra camera (Fig. 3.1) [51, 44]. The typical progression of the main parameters during a discharge are shown in Fig. 2.3.

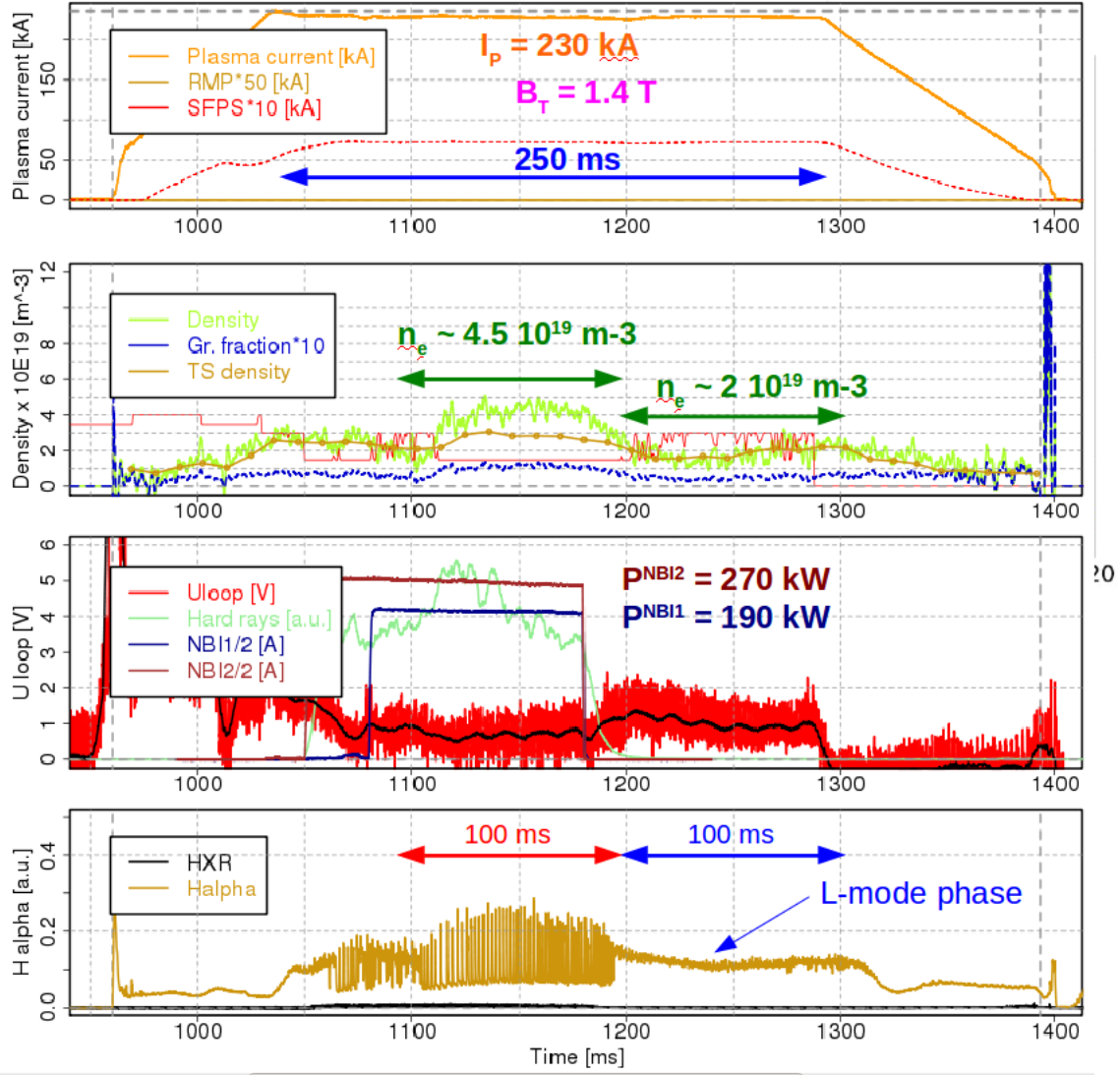


**Fig. 2.3:** Temporal evolution of the main parameters of a typical discharge in the experimental campaign. Taken from [3].

## 2.2 Experimental results

### 2.2.1 Lithium target

The lithium target was successfully exposed to 18 L-mode discharges with insertion up to 7.5 mm and 6 ELMy H-mode discharges with insertion up to 4 mm with no apparent damage. The target successfully survived steady state heat flux  $q_{\text{dep}} = 16 \text{ MW/m}^2$ . However the discharges were not long enough to heat up the target to sufficient temperature to achieve equilibrium of heating and vapor cooling. The temperature required according to preliminary simulations is  $T_{\text{Li}}^{\text{eq}} > 750 \text{ }^\circ\text{C}$  [1]. The maximum temperature measured (during discharge #19781, L-mode,  $z=7.5 \text{ mm}$ ) was  $T_{\text{surf}} = 400 \text{ }^\circ\text{C}$ , but the infrared camera was saturated. According to simulations of this discharge, the temperature was  $T_{\text{surf}}^{\text{sim}} \approx 650 \text{ }^\circ\text{C}$ .

After being inserted to 3.5 mm above the divertor tiles for ELMy H-mode exposure, the target was damaged. Due to local depletion of liquid lithium on the surface of the target, the top layers

of the molybdenum mesh were melted away (Fig. 5.3). The reason for the depletion is unknown however several possibilities are discussed in [7].

Throughout the campaign formation of liquid droplets on the surface was observed. These droplets were moving across the surface and eventually ejected from the sides of the target. The formation and subsequent ejection was allowed by an oxidized layer formed on the surface of the target (Fig. 2.4).

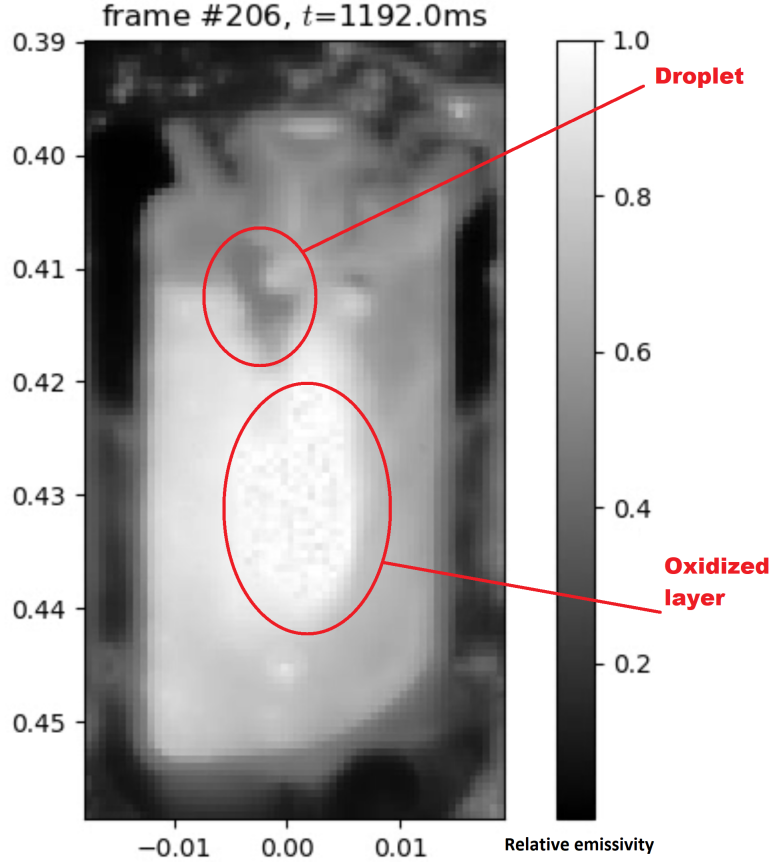


**Fig. 2.4:** Infrared camera photograph of the lithium target with captured droplet in the process of ejection and the oxidized layer.

According to calculations presented in [5] and shown in Fig. 2.5, for vertical ejection of droplets and overall MHD instability of the liquid the currents generated in the target (with toroidal field  $B_t = 1.4$  T) would have to be two orders of magnitude higher. For peak saturation current  $j_{\text{sat}}^{\text{elm}} = 163$  kA/m<sup>2</sup> measured by probes during discharge #19925 (SnLi campaign, H-mode) instability would occur for pore sizes  $> 2$  mm, which is more than 26 times the actual size. During a disruption in discharge #19873  $j_{\text{sat}}^{\text{dis}} = 206$  kA/m<sup>2</sup> was measured. The actual value of the current was most likely higher due to saturation of the measuring probe, but not by two orders of magnitude, the required value for instability. These observations show that the used CPS technology is from the point of MHD stability sufficient not only for the experiments on COMPASS but for possible future experiments on COMPASS-U, according to predicted parameters of discharges (3 times higher density, temperature and toroidal magnetic field).

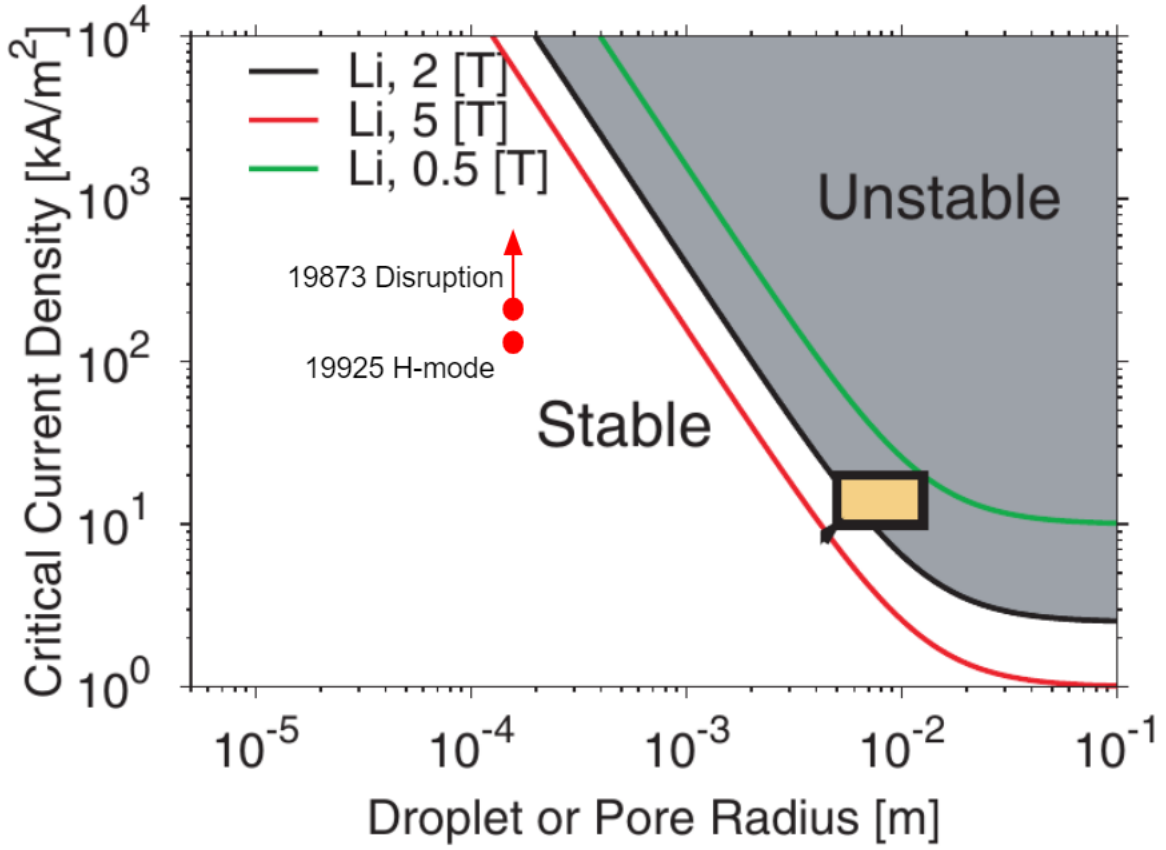


**Fig. 2.5:** Calculated limit of current densities and pore sizes for MHD stability of CPS modules with marked values measured during the SnLi campaign. Taken and edited from [5]

In total about 1 gram of lithium was released from the target. Mostly in the form of droplets. The splashed lithium deposited in the close vicinity of the target (Fig. 5.3). These droplets could cross separatrix and therefore pollute plasma with Li atoms. Even with excessive Li release disruptions due to radiation heat loss did not occur.

### 2.2.2 Tin-lithium target

The tin-lithium target BNC bulk construction allowed much higher surface temperatures to be reached, with smaller insertion. The highest surface temperature during discharge #19925, stable ELMy H-mode with 2.5 mm insertion (highest value), measured by infrared camera was  $T_{\text{SnLi}}^{\text{IR}} = 950\text{ }^{\circ}\text{C}$ . The surface temperature time evolution for various H-mode discharges measured by 4 kfps infrared camera is shown on Fig. 2.6. The measurements show, that each individual ELM, heats the target by  $\approx 45\text{ }^{\circ}\text{C}$ . The different temperature evolution in discharge #19917 is possibly due to divertor geometry caused shading.

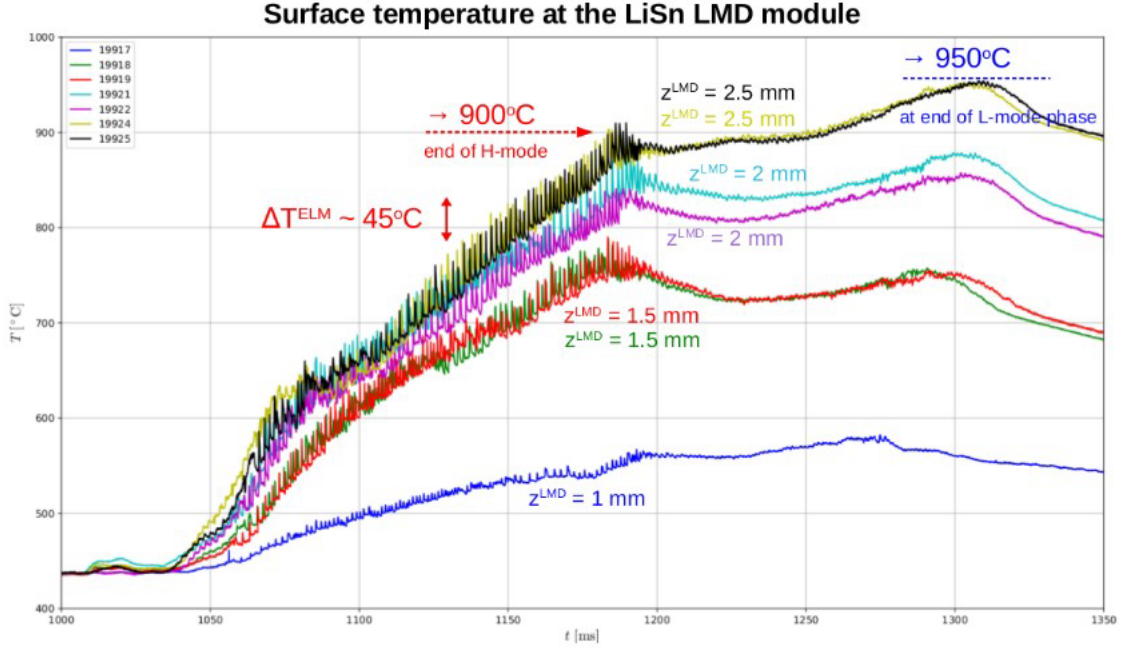


**Fig. 2.6:** Surface temperature evolution for H-mode discharges in SnLi campaign measured by 4 kfps infrared camera. Taken from [3].

According to simulations the lower particle exhaust of this alloy yields vapor cooling equilibrium temperature of  $T_{\text{SnLi}}^{\text{eq}} > 1000$  °C. Due to possible tin exhaust, that would disable tokamak operations, discharges with higher insertion were not conducted. During the discharges conducted, no surface droplets were observed. This would support the hypothesis, that droplet formation is possible with solid oxidized layer present on the surface. Spectroscopy measurements did not observe any tin in the plasma. Preference of lithium in sputtering events and lower evaporation pressure of tin combined with higher tin prompt redeposition fraction would indicate negligible tin release. It is however necessary to subject this to further research. The complete results overview of notable discharges is summarized in Tab. 2.1.

Discharge number	19781	19803	19805	19925
Diverted plasma mode	L	unstable H L	unstable H L	ELMy H (0.1 s)
Insertion [mm]	7.5	4	5	2.5
Liquid metal	Li	Li	Li	SnLi
Bulk material	Mo	Mo	Mo	BNC
Max. $\sin(\alpha)$	0.75	0.57	0.63	0.46
$q_{\text{dep}}$ [MW/m <sup>2</sup> ] peak effective	18 17	18 12	18 12	15 12
Max. $T_{\text{surf}}$ [°C] IR simulation	saturated 650	saturated 520	2600 visible camera	900 850

**Tab. 2.1:** Summary of results from notable discharges during Li a SnLi campaigns.

## 3. Vapor shielding model

For the purposes of the liquid metal experimental campaigns at the COMPASS tokamak a 3D heat model has been developed. This model consists of 3D heat diffusion in the target based on the heat transport equation and sputtering and evaporation of the plasma facing material [1]. Several corrections based on recent observations and simulations have been made which are discussed in 3.2.

### 3.1 3D Heat Transport model

The 3D Heat transport model consists of two parts. One is three dimensional thermal diffusion based on the thermal conduction equation and cooling effects of particle release (sputtering and evaporation). The simulated target is divided into finite number of block of constant temperature. The input onto the model is perpendicular heat flux  $q_{\perp}(x, y, t)$  where the  $x$  coordinate corresponds to radial position and  $y$  to insertion position of the block.

#### 3.1.1 Thermal diffusion

$$\frac{\partial T}{\partial t} = -\frac{1}{c_v} \nabla(\nabla(\kappa T)), \quad (3.1)$$

where  $T$  is temperature,  $c_v$  is volumetric heat capacity and  $\kappa$  is heat conduction [23, 47].

#### 3.1.2 Vapor cooling effects

The effects of particle exhaust on surface temperature are incorporated as a correction of heat flux  $q$ . The cooling power is calculated as a product of particle exhaust flux and cooled energy per particle.

$$q' = q - (\Gamma_{\text{sp}} + \Gamma_{\text{vap}})(1 - R)(\epsilon_{\text{cool}} + E_{\text{vap}}). \quad (3.2)$$

$\Gamma_{\text{sp}}$  is the flux of sputtered particles,  $\Gamma_{\text{vap}}$  is the flux of evaporated particles,  $R$  is prompt redeposition coefficient  $\epsilon_{\text{cool}}$  is energy cooled by line radiation in the neutral cloud per released particle and  $E_{\text{vap}}$  is the latent heat of evaporation per released particle. This is the equation presented in [1] as the basis for vapor cooling calculations. However later findings resulted in corrections which are discussed in section 3.2. [2].

## 3.2 Corrections in the model

### 3.2.1 Vapor Cooling

On the basis of the past experiment and new findings, several corrections to the model were made. Most notably, the calculation of cooling power itself was divided into local and global parts. Based on the observation of spherical cloud of  $\approx 10$  cm diameter, visible on Fig.5.1, the calculation of cooling power was divided into local cooling  $q_{\text{loc}}$  which is equal to latent heat of exhausted particles.

$$q_{\text{cool}}^{\text{loc}} = E_{\text{lat}}(\Gamma_{\text{sp}} + \Gamma_{\text{vap}}). \quad (3.3)$$

And into global cooling  $q_{\text{glob}}$  which is equal to line radiation cooling and calculated as

$$q_{\text{cool}}^{\text{glob}} = \int_S (\Gamma_{\text{sp}} + \Gamma_{\text{vap}}) \epsilon_{\text{cool}} \frac{dS}{\pi L_{\text{mfp}}^2}, \quad (3.4)$$

where  $S$  is the target surface, and  $L_{\text{mfp}}^2 \approx 6$  cm is the ionization mean free path (consistent with neutral cloud observation and BIT1D simulations). Latent heat of evaporation is taken from the exact point the exhausted particle left the surface, therefore it is strongly local. However randomness of the direction the exhausted particle travels to and randomness in radiative cooling exact position lead to possible cooling in a different area, than the area the particle was exhausted from. So the reason for the correction on global cooling is the size of the neutral cloud and the fact, that in case of divertor plasma, thermal footprint is strongly localized.

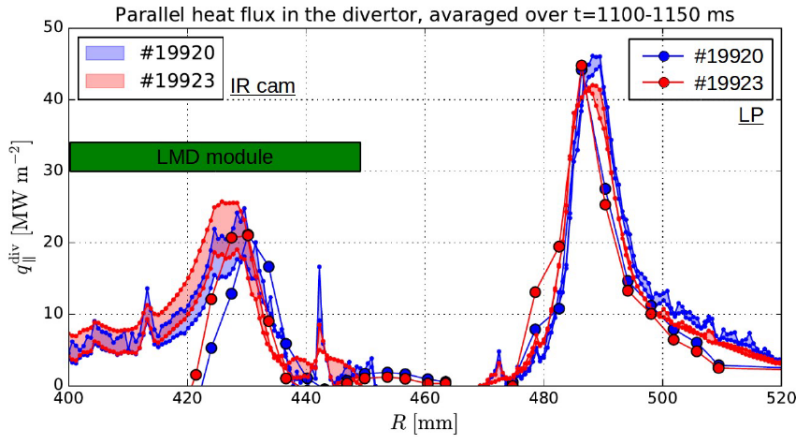


**Fig. 3.1:** Parallel heat flux in the divertor, averaged over  $t=1100-1150$  ms for discharges #19920 and #19923 measured by infrared camera and divertor probe field. Taken from [3].

The heat flux decay length  $\lambda_q$  is in range of several mm for COMPASS [51], so with strike point shifting during the discharges the total size of the thermal footprint is approximately 20 mm. This is visible from heat flux measurements on Fig. 3.1. The hot spot with strong evaporation radius of  $r^{\text{vap}} \approx 4$  mm and radius of the cloud  $r_{\text{cl}} \approx 6$  cm result in less than 1% of the radiation cooling occurring in the heated area. The rest of the radiation cooling happens in areas with no heat flux, where it is not needed.

### 3.2.2 Lithium prompt Redeposition

Kinetic simulations of lithium transport in the vicinity of the target conducted in the BIT1D Particle in Cell Monte Carlo code [4] yield negligible prompt redeposition of lithium atoms  $R \approx 0$ . This is due to the Li ionization front being above  $\text{Li}^+$  gyro-radius of  $\approx 30 \mu\text{m}$  and the magnetic presheath  $< 1 \text{ mm}$  as seen in Fig. 3.2. This result is in direct contradiction with results presented in [1], where three scenarios of  $R = 0.1; 0.9; 0.99$  were examined. [2]

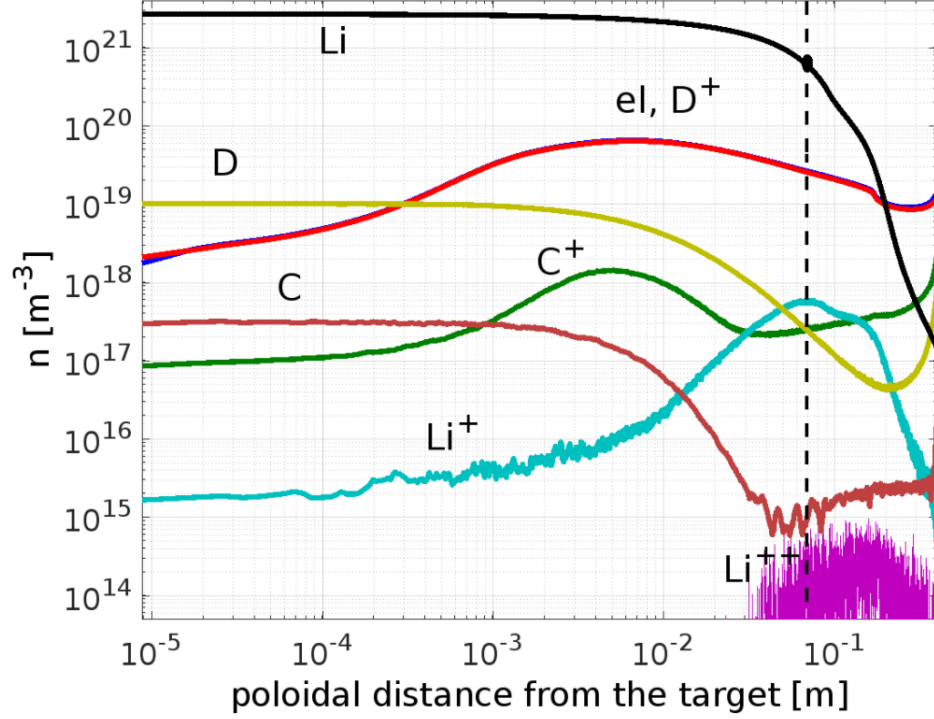


**Fig. 3.2:** The resulting concentrations of various components in the vicinity of the target from the BIT1D simulation [4]. Taken from [2].

Furthermore the simulation predicts neutral lithium cloud radius of  $L_{\text{Li}} \approx 6 \text{ cm}$ , black dashed line on Fig. 3.2. This is consistent with the observations from visible camera which give lithium cloud radius of  $r_{\text{Li}} \approx 6 \text{ cm}$ .

### 3.3 Tin-lithium experiment simulations

The model presented in [1] and discussed in this chapter was used in preliminary simulations only for the pure lithium experiment. It was therefore necessary to incorporate the effects of tin presence. Due to its much higher nucleon number and higher melting point than lithium 1.3, the exhaust of tin will be much lower than of lithium. In case of sputtering as shown of Fig. 3.3, the sputtering yield of tin by deuterium is in COMPASS relevant range of several eV to lower tens of eV, more than three orders of magnitude lower, therefore negligible. As tin has high prompt redeposition fraction, due to its mass, this may not be the case for self sputtering, however as sputtering is in comparison to evaporation orders of magnitude lower at higher temperatures even for lithium [1], this was for simplicity neglected.



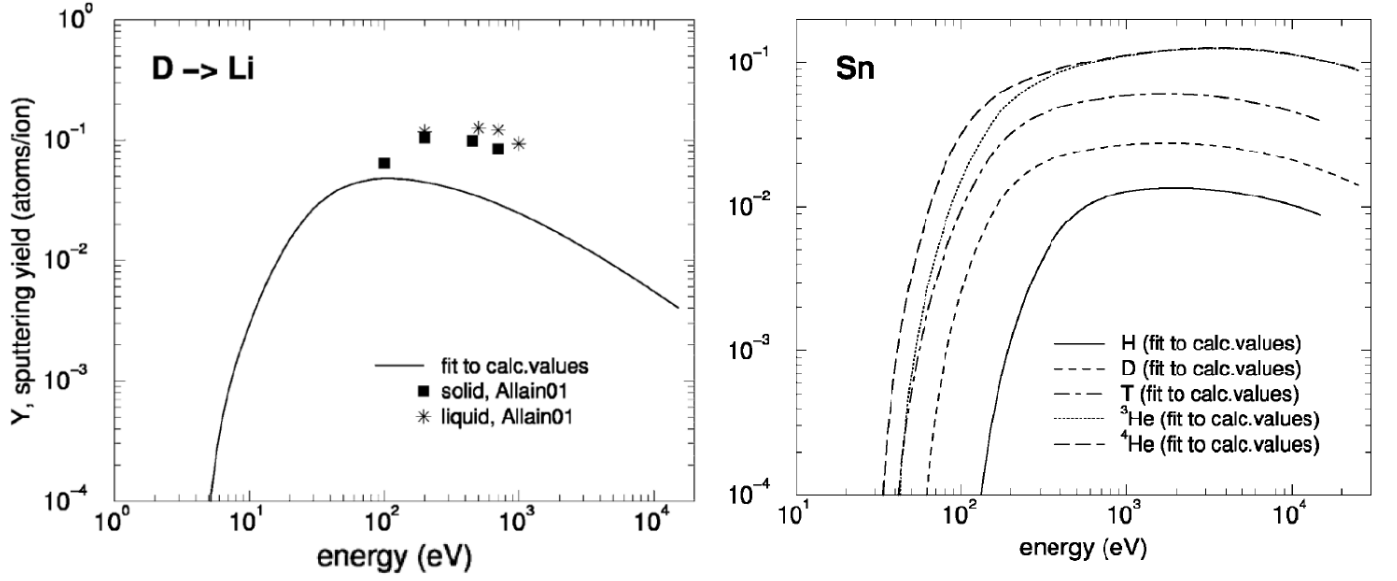


**Fig. 3.3:** Physical sputtering yields of lithium and tin as functions of incident particle energy. Taken from [33].

According to [30], the tin evaporation rate is 5-10 orders of magnitude lower than of lithium at the same temperature in temperature range of 200-1000 °C (Fig. 3.4). In case of SnLi alloy (75% Sn and 25% Li), the resulting effect is effectively lowered evaporation rate and strong dominance of exhausted lithium. As tin  $\epsilon_{\text{cool}}^{\text{tin}}$  vapor cooling energies are unknown and the exhaust is minuscule, it was assumed in the simulations, that only lithium is exhausted. This simplification is supported by no tin lines observations by spectroscopy.

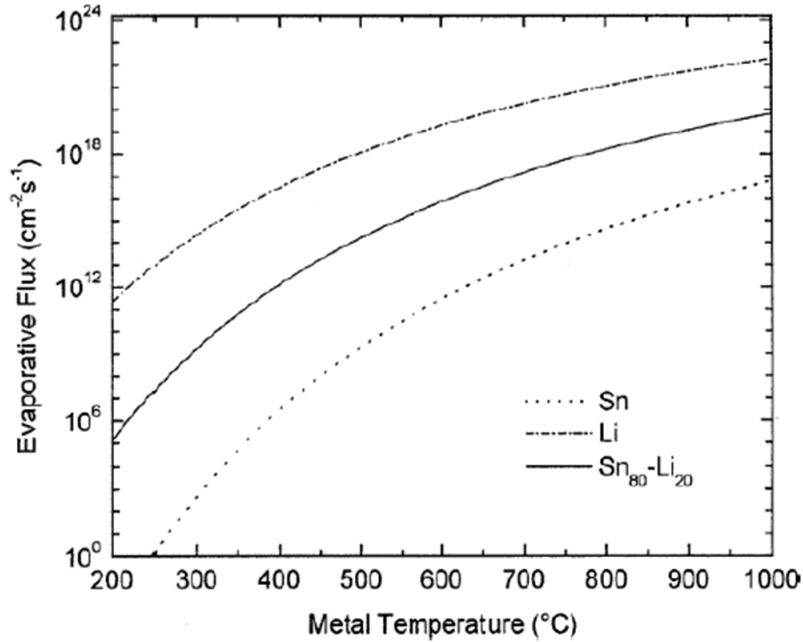


**Fig. 3.4:** Evaporation rate of pure Li, Sn and 80%Sn-20%Li alloy as functions of surface temperature. Taken from [30].

### 3.4 Simulation of discharge #19925 and comparison with experimental results

The quality and precision of the model can be best shown on simulations of discharge #19925, the discharge with the deepest insertion  $z^{\text{LMD}} = 2.5$  mm in the SnLi campaign. Because it serves as a basis for proposition of a next campaign, the simulations were tuned thoroughly. The resulting iteration of the model can be used for other scenarios in the future. The most important outputs of the simulation are shown on Fig. 3.5.

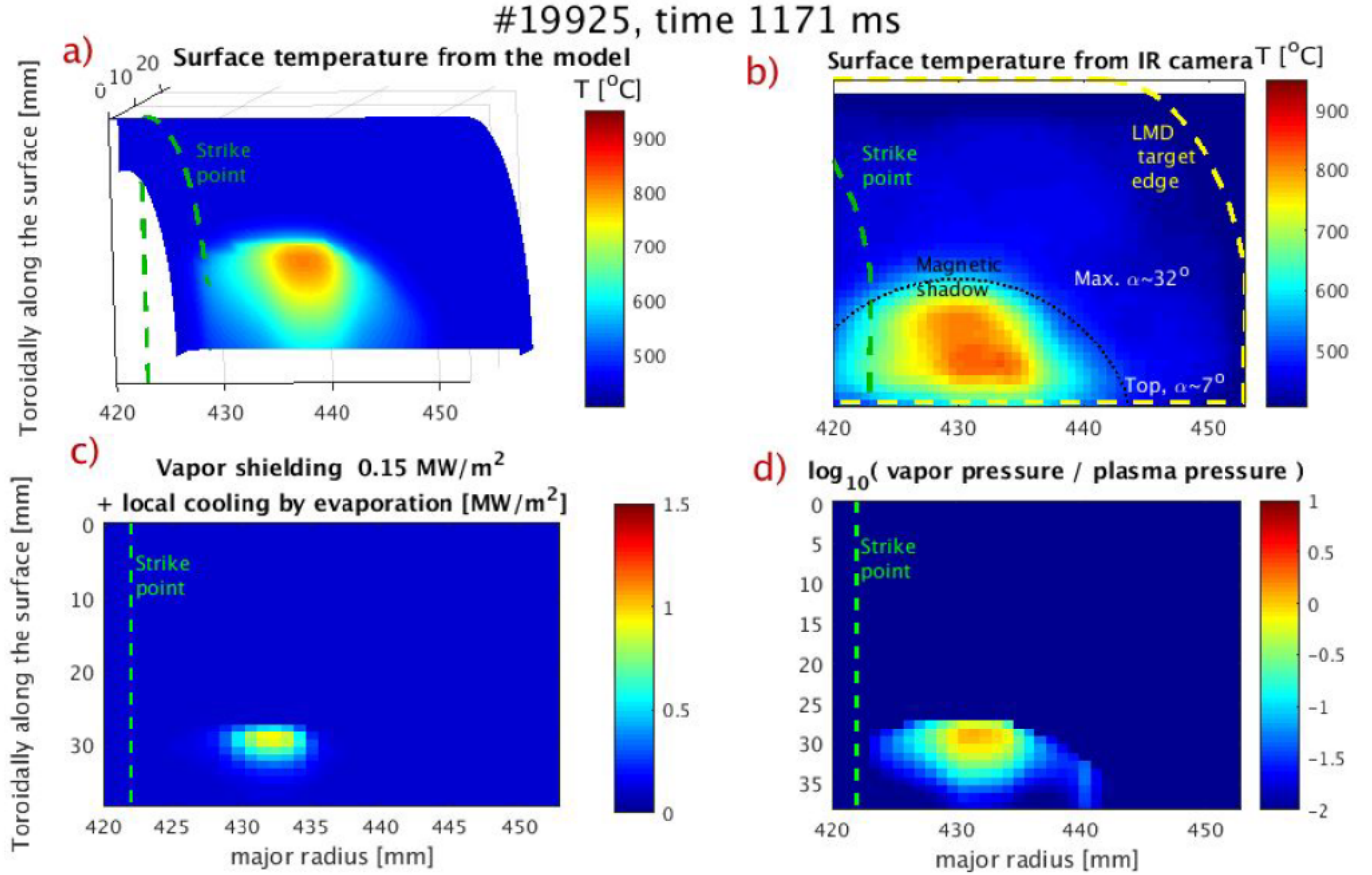


**Fig. 3.5:** a) Surface temperature of the target from the simulation at the end of H-mode. b) Surface temperature of the target from IR camera at the end of H-flux with PFCFLUX estimated magnetic shadow. c) Vapor cooling power at the end of H-mode. d) Vapor/plasma pressure fraction at the end of H-mode. Taken from [2].

In Fig. 3.5a the resulting surface temperature of the target in discharge #19925 (SnLi,  $z^{\text{LMD}} = 2.5$  mm) according to the simulation is shown. If compared to the infrared camera measurement of the same discharge in Fig. 3.5b a qualitative agreement in the maximal surface temperature is noticeable. However there is a discrepancy of surface temperatures at the edge of the target. In that area  $\sin(\alpha)$  is close to zero. The model therefore expects no temperature raise, but the infrared camera observes strong heating. This phenomenon has been observed in all discharges and is likely caused by short but significant preheating of the target top by the discharge beginning limited plasma when heat flows from the opposite toroidal direction and the ion Larmor smoothing

around the target magnetic shadow, which are not simulated [2]. The best correlation of the model with measurements was achieved with target inclination of  $7^\circ$ , which indicates that the target was indeed not installed perfectly in parallel to the divertor. The inclination of the target is however not a problem for the experiment itself, but only for simulations.

The simulation also shows a  $1\text{ MW/m}^2$  local evaporation cooling at the hot spot (Fig. 3.5c). This is approximately 6 times more than the global vapor cooling of  $\approx 0.15\text{ MW/m}^2$ . The energy cooled per particle is greater for the later. For example in case of lithium the latent heat is  $E_{\text{LHV}}^{\text{Li}} = 1.41\text{ eV}$  and radiation cooling in this scenario is  $E_{\text{rad}}^{\text{Li}} \approx 10\text{ eV}$  [1]. This shifts the equilibrium temperature to higher values and could be a problem for LMD performance in diverted plasmas. In Fig. 3.5d the vapor/plasma pressure fraction shows, 3 times higher Li pressure meaning lithium propagation against plasma stream.

As shown in Fig. 3.6 the evolution of the simulated maximal surface temperature of the target matches the infrared camera measurements even with the  $\Delta T_{\text{surf}} \approx 30^\circ\text{C}$  temperature raise during each individual ELM. This was achieved only with an assumption of a approximately  $100\text{ }\mu\text{m}$  poorly conductive surface layer on top of the  $1\text{ mm}$  CPS layer, with heat transmission coefficient of  $1\text{ MW/m}^2/\text{K}$  [6]. A simulation ran without this assumption resulted in ELM temperature raise of only few degrees Celsius.

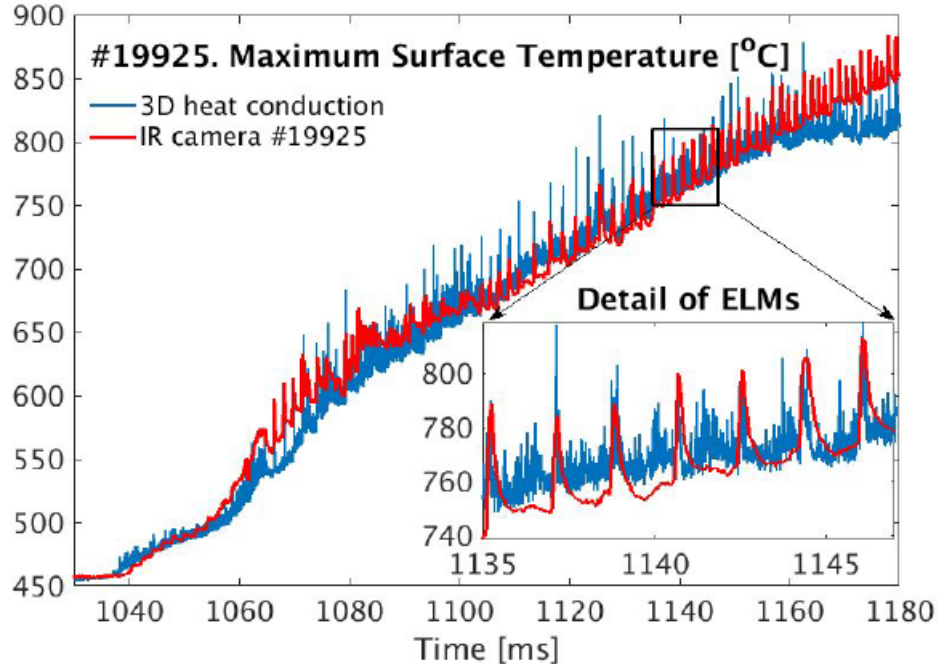


**Fig. 3.6:** Time evolution of the maximal LMD target surface temperature in discharge #19925 from simulation and IR camera measurement. Taken from [2].

Though the surface temperatures achieved with the SnLi target were approximately  $900^\circ\text{C}$  (Fig. 2.6) at the end of stable ELMy H-mode, which for pure lithium should be enough for surface temperature saturation, for SnLi this was not the case as the vapor cooling was  $q_{\text{vap}} \approx 0.15\text{ MW/m}^2$  compared to the heating by plasma of  $q_{\text{heat}} = 12\text{ MW/m}^2$ . However because the SnLi target was constructed from BNC, the temperatures reached were achieved with much lower insertion than with pure lithium molybdenum target (Tab. 2.1). Therefore with deep insertion,  $z_{\text{SnLi}}^{\text{LMD}} = 7\text{ mm}$ , the SnLi target should reach temperature saturation. If vapor shielding effect would be significant, the saturation the temperature should be much lower than if the effect is minuscule. Simulations

of this scenario show a difference of  $\Delta T_{\text{surf}} \approx 200 \text{ }^{\circ}\text{C}$  (Fig. 3.7). Another experiment, where deep insertion to 8 mm will be performed should answer, whether the vapor shielding effect is present in this scenario or not.

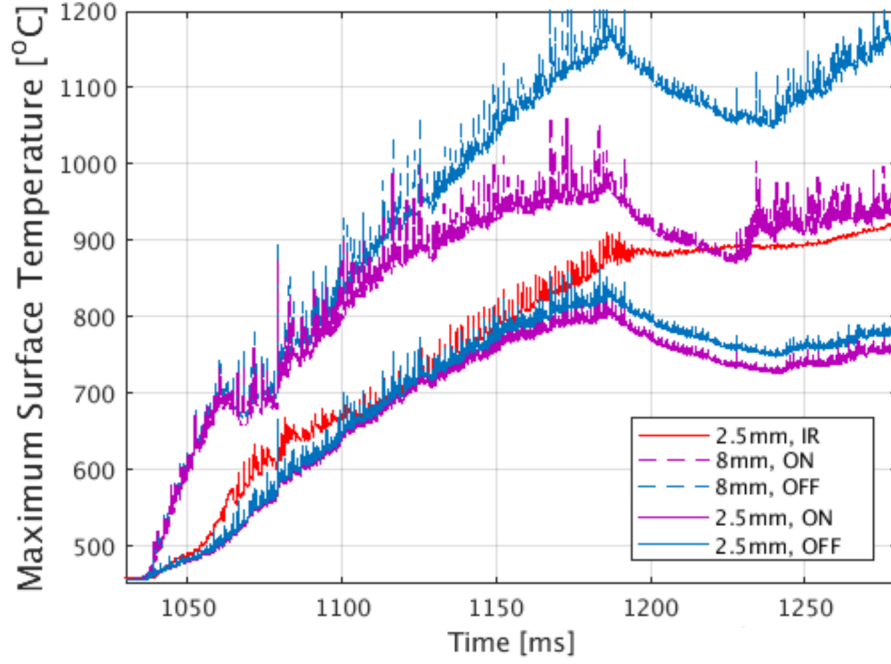


**Fig. 3.7:** Overview of surface temperature time evolution of discharge #19925 for  $z^{\text{LMD}} = 2.5 \text{ mm}$  infrared camera measurement (red), simulation with vapor cooling (violet), simulation without vapor cooling (blue), simulation of the  $z^{\text{LMD}} = 8 \text{ mm}$  scenario for discharge #19925 with vapor cooling (dashed violet), and without vapor cooling (dashed blue).

## 4. Conclusion

Two LMD targets based on CPS technology with molybdenum mesh were exposed to diverted plasma in COMPASS tokamak. The first target, made with molybdenum bulk and wetted with lithium, successfully survived insertion by 7.5 mm above divertor tiles with effective deposited heat flux  $q_{\text{Li}}^{\text{L}} = 17 \text{ MW/m}^2$  in L-mode and by 4 mm with  $q_{\text{Li}}^{\text{H}} = 12 \text{ MW/m}^2$  in H-mode. No apparent influence on plasma performance was observed. When inserted to 5 mm above divertor tiles, with same discharge parameters, the top molybdenum mesh layer was melted away. The cause was however not high heat flux, as the target survived higher heat fluxes in previous discharges and enough lithium was left in the reservoir to prevent heating to molybdenum melting point.

During the discharges lithium droplets were ejected from the surface of the target. The ejection was possible because of an oxidized layer formed on the surface of the target. Measurements of grounded currents in the vicinity of the target and subsequent calculation of present forces showed the MHD stability limit of the target to be more than two orders of magnitude above measured values. The second target, made with BNC bulk and wetted with 27% Li and 73% Sn was successfully exposed to H-mode plasma with effective heat flux  $q_{\text{SnLi}}^{\text{H}} = 12 \text{ MW/m}^2$  with insertion by 2.5 mm. Due to the low heat conductivity of the bulk BNC, the maximal surface temperature reached  $T_{\text{surf}}^{\text{SnLi}} = 950 \text{ }^\circ\text{C}$ . For possible observation of vapor cooling equilibrium at  $T_{\text{eq}} = 1100\text{-}1350 \text{ }^\circ\text{C}$ , deeper insertion would have been required.

At the temperatures reached during the campaign tin evaporation rate is minuscule and with support by strong redeposition, the implication would be no tin release into plasma. This is in agreement with tin spectral lines not being observed during the campaign.

For the purpose of the target temporal and spatial temperature profiles with the inclusion of vapor cooling effects simulations a 3D heat transport model has been developed. Based on newly acquired knowledge corrections of the model were performed. No lithium redeposition was incorporated based on results of the kinetic PIC simulations in the BIT1D code of the particle fluxes in the vicinity of the target. According to observation of the neutral cloud cooling being strongly non-local the vapor cooling effect was divided into local part equal to latent heat of the exhausted particles and non-local part equal to radiation of a 12 mm wide neutral cloud.

The experimental results show, both Li and SnLi wetted CPS can survive 0.1 s H-mode plasma with heat fluxes up to  $12 \text{ MW/m}^2$  and no active cooling. However for clear determination of the vapor cooling effect, deeper insertion would be required. The viability of this technology as a divertor concept in ITER or DEMO like reactors, will not be decidable without further experimental research including higher heat fluxes, longer exposures and ideally active cooling of the tested target.

## 5. Attachment

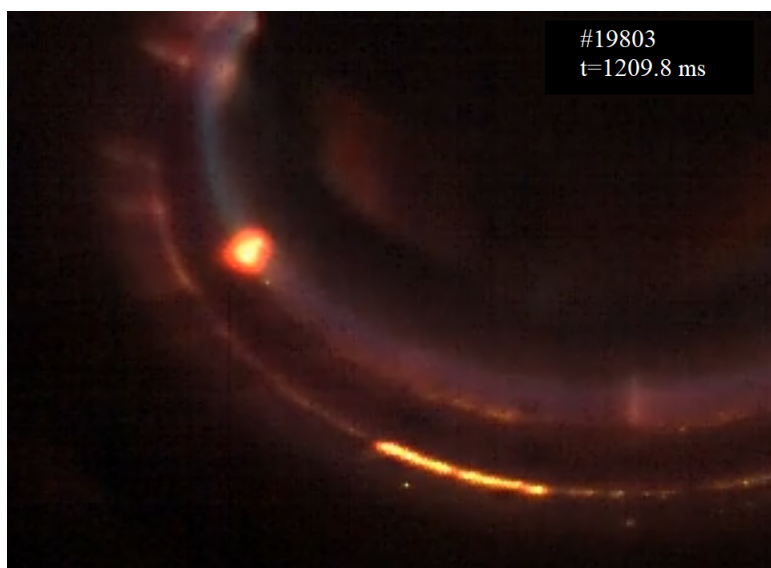
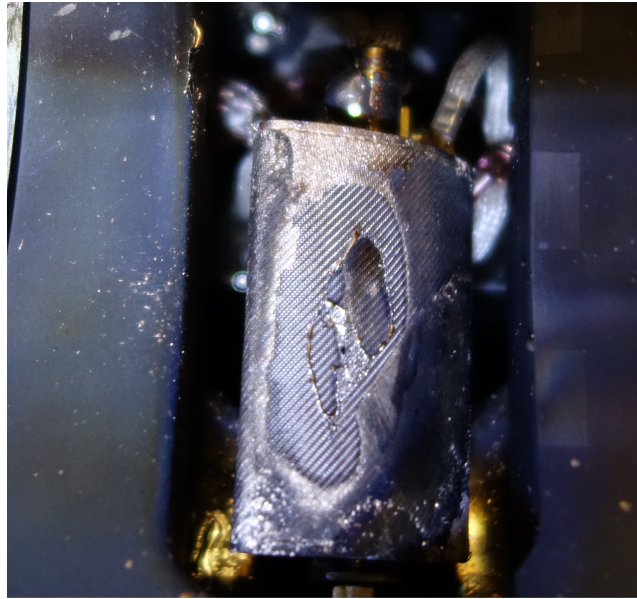


**Fig. 5.1:** Image from the visible camera of discharge #19083 at  $t = 1209.8$  ms.



**a)**



**b)**

**Fig. 5.2:** a) Photograph of the lithium target after installation, before the campaign. b) Photograph of the lithium target after the campaign.



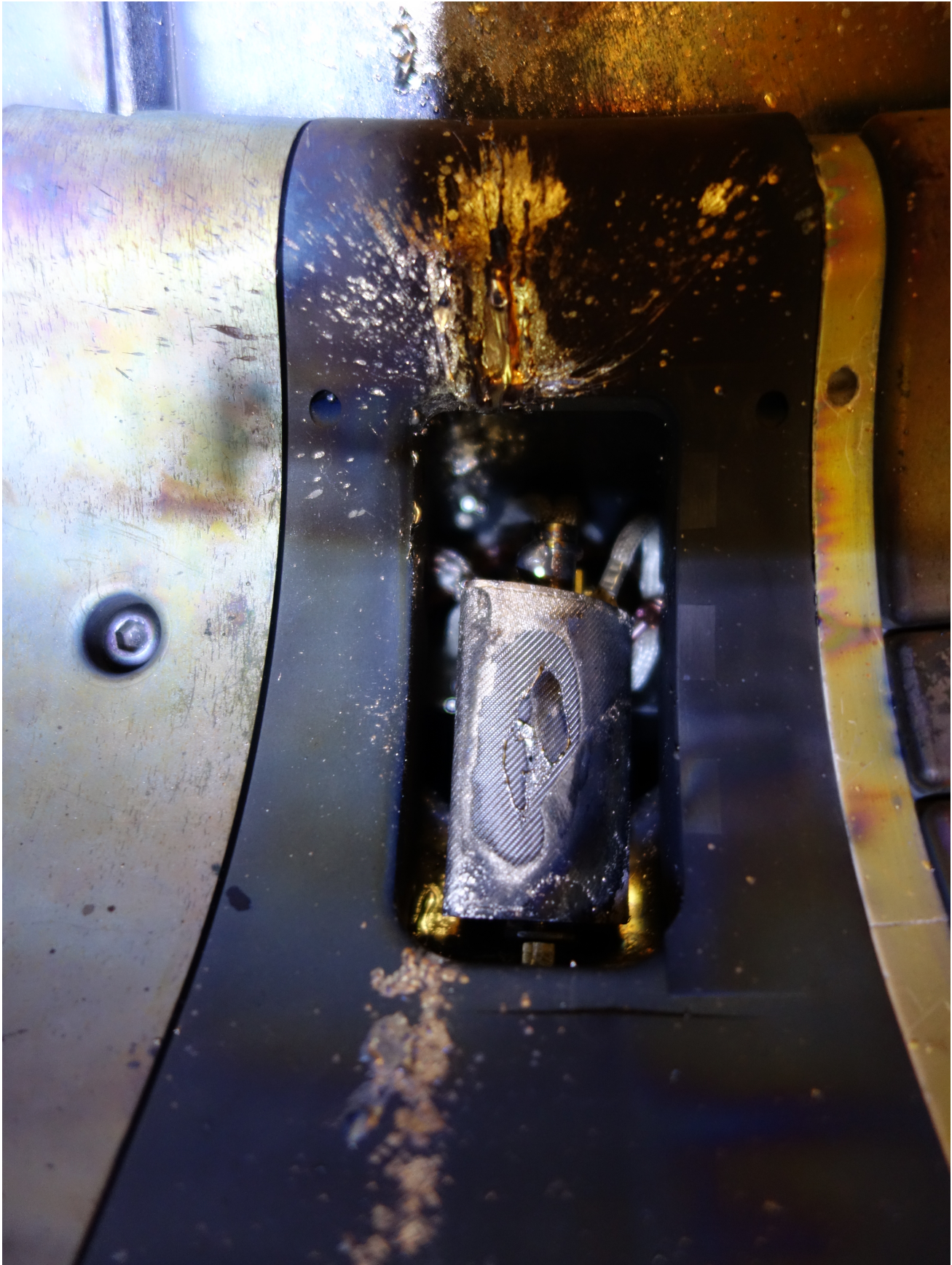


**Fig. 5.3:** Photograph of the damaged lithium target and the surrounding divertor tiles.



# Bibliography

- [1] CECRDLE, J. *První experiment s tekutým lithiem na divertoru tokamaku COMPASS*. Bc. thesis, Faculty of Nuclear Sciences and Physical Engineering, Czech Technical University in Prague, 2019
- [2] HORACEK, J. et al. *Modeling of COMPASS tokamak divertor liquid metal experiments* Submitted to: Nuclear Material and Energy, 2020
- [3] DEJARNAC, R. et al. *Overview of power exhaust experiments in the COMPASS divertor with liquid metals* Submitted to: Nuclear Material and Energy, 2020
- [4] TSKHAKAYA, D. et al. *Modelling of tungsten re-deposition coefficient* Journal of Nuclear Materials, 2014, Vol. 463
- [5] JAWORSKI, M. A. et al. *Liquid lithium divertor characteristics and plasma-material interactions in NSTX high-performance plasmas*. Nuclear Fusion, 2013, Vol. 53
- [6] VONDRACEK, P. et al. *Divertor infrared thermography on COMPASS*. Fusion Engineering and Design, 2019, Vol. 146
- [7] LUKES, S. *Analyza prvního experimentu s tekutými kovy na divertoru tokamaku COMPASS*. Bc. thesis, Faculty of Nuclear Sciences and Physical Engineering, Czech Technical University in Prague, 2020
- [8] LIAO, CH., Kazimi M. S, *On the Design of Liquid Metal Divertors*
- [9] ZOHN, H. *Magnetohydrodynamic Stability of Tokamaks* John Wiley & Sons, Incorporated, 2015. Available from: ProQuest Ebook Central, [10.9.2020] <https://ebookcentral.proquest.com/lib/cvut/detail.action?docID=1873195>.
- [10] CONNOR, J. W. et al. *Magnetohydrodynamic stability of tokamak edge plasmas*. Physics of Plasmas, 1998, Vol. 5., Num. 7.
- [11] PITTS, R.A. et al. *Physics conclusions in support of ITER W divertor monoblock shaping*. Nuclear Materials and Energy, 2017.
- [12] MITTEAU, R. et al. *The design of the ITER first wall panels*. Fusion Engineering and Design, 2013, Vol. 88.
- [13] KULHÁNEK, P. *Uvod do teorie plazmatu*. 1st ed. Praha: Aldebaran Group for Astrophysics, 2011. ISBN 978-80-904582-2-2.
- [14] PITTS, R. et al. *Fusion - The Way Ahead*. Physics World, 2006, Vol. 19 (3) 20.

- [15] MCCRACKEN, Garry M. and Peter E. STOTT. *Fusion: The Energy of the Universe*. Amsterdam: Elsevier Academic Press, 2005. ISBN 0-12-481851-X.
- [16] KEILHACKER, M. *H-mode confinement in tokamaks*. Plasma Physics and Controlled Fusion, 1987, Vol. 29, No. IOA, pp. 1401 -1413.
- [17] STACEY, Weston M. *Fusion plasma physics*. Weinheim: Wiley-VCH, 2005. ISBN 3-527-40586-0.
- [18] Department of Physics, University of York, *The influence of magnetic geometry on the plasma edge region of future fusion reactors*. [online], [cit. 13.5.2019], Dostupné z: <https://www.york.ac.uk/media/physics/ypi/optimising%20future%20fusion%20energy%20reactors.jpg>
- [19] PITTS, R.A. etal., *A full tungsten divertor for ITER: Physics issues and design status*. Journal of Nuclear Materials 438 2013 S48–S56.
- [20] FARREL, K. etal., *Recrystallization, grain growth and the ductile-brittle transition in tungsten sheet*. Journal Of the Less-common Metals, 1967, Vol. 13 No. 2, pp. 141-155.
- [21] LEONARD, A.W., *Plasma detachment in divertor tokamaks*. Plasma Physics and Controlled Fusion, 2018, Vol. 60.
- [22] PETRIE, T.W. etal. *RADIATIVE DIVERTOR EXPERIMENTS IN DIII-D WITH D2 INJECTION*. Nuclear Fusion, 1997, Vol. 37
- [23] HORACEK, J. etal., *Plans for Liquid Metal Divertor in Tokamak Compass*. Plasma Physics Reports, 2018, Vol. 44, No. 7, pp. 652–656.
- [24] COENEN, J.W. etal. *ELM-induced transient tungsten melting in the JET divertor* Nuclear Fusion, 2015, Vol. 55.
- [25] HORACEK J. etal., *Feasibility study of fast swept divertor strike point suppressing transient heat fluxes in big tokamaks* Fusion engineering and Design, 2017, Vol. 123.
- [26] PANEK, R. etal. *Status of the COMPASS tokamak and characterization of the first H-mode*. Plasma Physics and Controlled Fusion, 2015, Vol. 58, No. 1.
- [27] Institute of Plasma Physics, Czech Academy of Sciences, *Tokamak COMPASS*. [online], [cit. 31.5.2019], Available from: [http://www.ipp.cas.cz/miranda2/export/sitesavcr/ufp/sys/galerie-obrazky/COMPASS\\_at\\_IPP\\_left.jpg](http://www.ipp.cas.cz/miranda2/export/sitesavcr/ufp/sys/galerie-obrazky/COMPASS_at_IPP_left.jpg)
- [28] MIKULCAK, J., etal. *Matematicke, fyzikalni a chemicke tabulky pro stredni skoly*. 1st ed. Praha: SPN, 1988. 54-09-12/1b.
- [29] EVTIKHIN, V.A., etal. *Lithium divertor concept and results of supporting experiments*. Plasma Physics and Controlled Fusion, 2002, Vol. 44.
- [30] TABARÉS, F. L., etal., *Reactor plasma facing component designs based on liquid metal concepts supported in porous systems*, Nuclear Fusion, 2017, Vol. 57.
- [31] RUMBLE, John R., ed., David R. LIDE, ed. a Thomas J. BRUNO, *CRC handbook of chemistry and physics: a ready-reference book of chemical and physical data*. 99th edition. Boca Raton: CRC Press, Taylor & Francis Group, 2018, ISBN 978-1-138-56163-2.

- [32] SMITH, R.L., *Compilation of the properties of lithium hydride*. Washington, United States, NASA, 1963, Doc. ID: 19720066808.
- [33] BEHRISCH, R., ECKSTEIN, W., *Sputtering by Particle Bombardment: Experiments and Computer Calculations from Threshold to MeV Energies*. Topics in applied physics 110. Berlin: Springer Verlag. 2007. ISBN 987-3-540-44500-5.
- [34] SCHERBAK, A. N. et al., *Experiments on the Capture of Li, H, and D by Lithium Collectors at Different Surface Temperatures at the T-11M Tokamak*. Plasma Physics Reports, 2018, Vol. 44.
- [35] LANGMUIR, I., *Condensation and Evaporation of Gas Molecules*. Monthly Weather Review, 1917, Vol. 45, p. 452.
- [36] MORGAN, T.W. et al., *Interaction of a tin-based capillary porous structure with ITER/DEMO relevant plasma conditions*. Journal of Nuclear Materials, 2015, Vol. 463.
- [37] ABRAMS, T.W., *Erosion and Re-deposition of Lithium and Boron Coatings Under High-Flux Plasma Bombardment*. Ph.D. thesis, Princeton University, 2015.
- [38] DOERNER, R.P. et al., *Measurements of erosions mechanisms from solid and liquid materials in PISCES-B*. Journal of Nuclear Materials, 2001 Vol. 166.
- [39] GOLDSTON, R.J. et al., *Recent advances towards a lithium vapor box divertor*. Nuclear Materials and Energy, 2017, Vol. 12.
- [40] RINDT, P. et al., *Power handling limit of liquid lithium divertor targets*. Nuclear Fusion, 2018, Vol. 58.
- [41] NYGREN, R.E a Tabares, F.L., *Liquid surfaces for fusion plasma facing components—A critical review. Part I: Physics and PSI*. Nuclear Materials and Energy, 2016, Vol. 9.
- [42] ALCOCK, C.B, Itkin V. P. a Horrigan M. K. *Vapour Pressure Equations for the Metallic Elements: 298–2500K*. Canadian Metallurgical Quarterly, 1984, Vol. 23.
- [43] TSKHAKAYA, D., *Modelling of tungsten re-deposition coefficient*. Journal of Nuclear Materials, 2015, Vol. 463.
- [44] VONDRÁČEK, P., *Plasma Heat Flux to Solid Structures in Tokamaks* Ph.D. thesis, Matematicko-fyzikální fakulta, Univerzita Karlova, 2019.
- [45] STANGEBY, P.C., (2000). *The Plasma Boundary of Magnetic Fusion Devices*. Institute of Physics Publishing, 2000, ISBN 0-7503-0559-2.
- [46] ADAMEK, J. et al., *Electron temperature and heat load measurements in the COMPASS divertor using the new system of probes*. Nuclear Fusion, 2017, Vol. 57.
- [47] WOLFF, A., *Heat conduction in the divertor target plate of the ITER tokamak*. Bc. thesis, Faculty of Nuclear Sciences and Physical Engineering, Czech Technical University in Prague, 2011.
- [48] PORADZINSKI, M. et al. *Integrated power exhaust modelling for DEMO with lithium divertor*. 2018, Submitted to Fusion Engineering and Design.

- [49] LYUBLINSKI, I. E. and A. V. Vertkov, *Comparative assessment of application of low melting metals with capillary pore systems in a tokamak*. Fusion Engineering and Design, 2014, Vol. 89.
- [50] PSHENOV, A. and A. S. Kukushkin, *SOLPS4.3 Modeling of Lithium Transport and Noncoronal Radiation in the T-15 Tokamak with Lithium Emitter-Collector Scheme in Use*. Plasma Physics Reports, 2018, Vol. 44.
- [51] ADAMEK, J. etal. *Fast measurements of the electron temperature and parallel heat flux in ELMy H-mode on the COMPASS tokamak*. Nuclear Fusion, 2016, Vol. 57.